Weyl semimetallic state with antiferromagnetic order in the Rashba-Hubbard model

Aastha Jain, Garima Goyal ⬤, and Dheeraj Kumar Singh

Department of Physics and Materials Science, Thapar Institute of Engineering and Technology, Patiala 147004, Punjab, India

We study the phase diagram of the Rashba-Hubbard model by employing the Hartree-Fock mean-field theory and thereby establish the existence of an antiferromagnetically ordered Weyl semimetallic state with in-plane magnetic moments. This phase is found to be sandwiched between the antiferromagnetic insulator and Rashba metal in the interaction vs spin-orbit coupling phase diagram. The antiferromagnetically ordered topological semimetallic state exists in the presence of combined time-reversal and inversion symmetry, although individually both are broken. The study of the static magnetic susceptibility indicates the robustness of the antiferromagnetic order within a realistic range of interaction and spin-orbit coupling parameters. In addition to the edge states associated with the Weyl points, we also investigate the spin-resolved quasiparticle interference, which provides important insight into the possible spin texture of the bands, especially in the vicinity of Weyl points.

I. INTRODUCTION

Different phases are classified according to the different symmetries that may spontaneously be broken at low temperature because of a variety of interactions inherent in material systems and that can lead to intriguing diverse phases and associated features [1–9]. One such important interaction, which has attracted considerable attention recently and which can profoundly affect the properties of various phases as well the nature of the phase transition, is spin-orbit coupling (SOC), i.e., the entanglement of spin and orbit degrees of freedom [10–12]. The investigation of proximity effects in heterojunctions of superconductors and magnetic systems suggests that SOC may play a critical role in shaping magnetic, transport, and other exciting properties [13–16]. The signature of nontrivial topological states accompanied by Majorana quasiparticles [17–21] was obtained in systems with SOC.

In two-dimensional systems, especially at the interface of heterostructures, the absence of inversion symmetry can generate SOC, which is referred to as Rashba SOC [22]. Rashba SOC depends linearly on the crystal momentum **k** and lifts the spin degeneracy of the energy bands and therefore can significantly influence the electronic and transport properties, giving rise to a wide variety of fascinating properties [23–25]. Moreover, by controlling the layer thickness of the heterostructure or through the application of an external electric field, the strength of Rashba SOC can be controlled, making such systems more suitable for several potential technological applications [26–32]. This is unlike centrosymmetric systems with transition metals as indispensable constituents, in which the SOC results from the LS coupling in the d and f orbitals.

The SOC in a correlated-electron system introduces quantum frustration, which, in addition to affecting the nature of the Mott transition, can stabilize a plethora of exotic states of matter. These states of matter can include axion insulators, spin-orbit coupled Mott insulators, topological semimetals and insulators, etc. [30,33–37]. However, in noncentrosymmetric systems, despite the significant progress made in understanding different aspects of Rashba SOC, relatively less attention has been paid to the consequences of its interplay with the electronic correlation. In a few steps taken in this direction, the nature of the metal-to-insulator transition (MIT) and the phase diagram in the Rashba-Hubbard model were studied by using a variety of methods, including the Hartree-Fock (HF) approximation [38], variational Monte Carlo (VMC) [39], and cluster dynamical mean-field theory (CDMFT) [40].

Sine-deformed mean-field theory based on the HF approximation predicts incommensurate spin-density wave (SDW) states even when the SOC is vanishingly small and spiral orders for larger SOC [41]. Other HF-based theories suggest that a metallic state with antiferromagnetic (AFM) order for moderate electronic correlation, an AFM insulator for strong electronic correlation, and a striped magnetic order when both SOC and electronic correlations being large, are stabilized [38]. The existence of AFM order for smaller SOC is also supported by CDMFT [40] as well as plaquette-based investigations [42]. VMC studies point out the existence of a Weyl semimetallic (WSM) state without AFM order for stronger SOC and electronic correlation [39]. Among the various phases thus found, the metallic AFM state appears to be of considerable interest, particularly given its pseudogaplike behavior. The current study attempts to provide a detailed investigation of this phase, most importantly, revealing its topological nature.

Our finding suggests that for a reasonable range of SOC and on-site Coulomb interaction, a significant portion of the SOC vs interaction phase diagram is occupied by the metallic and insulating AFM ordered states with in-plane magnetic moment. The transition from the Rashba metal to AFM insulator does not happen directly upon increasing the electronic correlation parameter U. Instead, a WSM state with

AFM order is stabilized between the two aforementioned phases. The associated Weyl points (WPs) shift from the high-symmetry points Γ and M in the paramagnetic Rashba metallic state to the points along the high-symmetry directions given by $\pm k_x \mp k_y = \pi$ and $k_x = -k_y$ in the WSM-AFM state. Their respective winding numbers are 1 and -1. We also examine the spin-resolved quasiparticle interference (QPI) patterns, which are capable of revealing the nature of electronic states, including the spin texture in the vicinity of the WPs.

The layout of this paper is as follows. Section II describes the Rashba-Hubbard Hamiltonian, mean-field Hamiltonian, static magnetic susceptibility calculation in the unordered state, and spin-resolved QPI. In Sec. III, the robustness of the AFM ordering, the phase diagram in the U-λ space, the necessary conditions for the WSM state, linearized dispersions near WPs, winding numbers and edge states associated with the WPs, and QPI patterns in the WSM-AFM state are presented. In Sec. IV, we provide a brief discussion in reference to previous works. Finally, we conclude in Sec. V.

II. MODEL AND METHOD

A. Model

We consider the one-orbital Rashba-Hubbard Hamiltonian defined on a square lattice, given by

$$\mathcal{H} = H_t + H_U + H_R, \tag{1}$$

where

$$H_t = -t \sum_{\langle \mathbf{i},\mathbf{j} \rangle} \sum_{\sigma} (d^{\dagger}_{\mathbf{i}\sigma} d_{\mathbf{j}\sigma} + \text{H.c.}) \tag{2}$$

is the kinetic energy term representing the delocalization energy gain due to the nearest-neighbor hopping. t is the hopping amplitude, and $d^{\dagger}_{\mathbf{i}\sigma}$ ($d_{\mathbf{i}\sigma}$) is the operator creating (annihilating) an electron at site $\mathbf{i}$ with spin σ. The unit of interaction parameters and energy is henceforth set to be t.

The second term,

$$H_U = U \sum_{\mathbf{i}} \hat{n}_{\mathbf{i}\uparrow} \hat{n}_{\mathbf{i}\downarrow}, \tag{3}$$

accounts for the on-site Coulomb repulsion between electrons of opposite spins, where $\hat{n}_{\mathbf{i}\sigma} = d^{\dagger}_{\mathbf{i}\sigma} d_{\mathbf{i}\sigma}$ denotes the number operator. The third term, H_R, represents the Rashba SOC, which is defined as

$$H_R = \lambda \sum_{\mathbf{i},\sigma,\sigma'} [i(d^{\dagger}_{\mathbf{i},\sigma} \sigma^x_{\sigma\sigma'} d_{\mathbf{i}+\hat{y},\sigma'} - d^{\dagger}_{\mathbf{i},\sigma} \sigma^y_{\sigma\sigma'} d_{\mathbf{i}+\hat{x},\sigma'}) + \text{H.c.}], \tag{4}$$

where λ is the strength of SOC and σ^i is one of the Pauli matrices.

After Fourier transformation, Eq. (2) in momentum space is given by

$$H_t(\mathbf{k}) = \sum_{\mathbf{k},\sigma} \epsilon_{\mathbf{k}} d^{\dagger}_{\mathbf{k}\sigma} d_{\mathbf{k}\sigma}, \tag{5}$$

with $\epsilon_{\mathbf{k}} = -2t(\cos k_x + \cos k_y)$, whereas the Rashba term [Eq. (4)] takes the following matrix form:

$$H_R(\mathbf{k}) = \sum_{\mathbf{k},\sigma,\sigma'} d^{\dagger}_{\mathbf{k}\sigma} [\beta_{\mathbf{k}} \sigma^x_{\sigma\sigma'} - \gamma_{\mathbf{k}} \sigma^y_{\sigma\sigma'}] d_{\mathbf{k}\sigma'}, \tag{6}$$

with $\beta_{\mathbf{k}} = 2\lambda \sin k_y$ and $\gamma_{\mathbf{k}} = 2\lambda \sin k_x$.

B. Hartree-Fock mean-field theory

The Hubbard term H_U, which is quartic in terms of electron-field operators, has been treated in the absence of Rashba SOC via a variety of techniques based on mean-field theoretic approaches, perturbation techniques, dynamical mean-field theory [43], quantum Monte Carlo [44], VMC [45], etc. Here, we use the static mean-field approach based on the Hartree-Fock approximation in order to decouple the interaction Hamiltonian because our focus is mainly on the low-temperature phases. The bilinear term in the electron-field operator thus obtained is

$$H_{im} = -\frac{U}{2} \sum_{\mathbf{i}\sigma} \psi^{\dagger}_{\mathbf{i}} (\sigma \cdot \mathbf{m_i}) \psi_{\mathbf{i}}, \tag{7}$$

where $\psi^{\dagger}_{\mathbf{i}} = (d^{\dagger}_{\mathbf{i}\uparrow}, d^{\dagger}_{\mathbf{i}\downarrow})$. The jth component of the magnetic moment at site $\mathbf{i}$ is $m^j_{\mathbf{i}} = \frac{1}{2} \langle \psi^{\dagger}_{\mathbf{i}} \sigma^j \psi_{\mathbf{i}} \rangle$, with $\mathbf{m_i}$ being the magnetic moment. σ^j is the jth component of the Pauli matrices. When the decoupled interaction term is incorporated, the Hamiltonian in the basis $(d_{\mathbf{k}\uparrow}, d_{\mathbf{k}\downarrow}, d_{\mathbf{k}+\mathbf{Q}\uparrow}, d_{\mathbf{k}+\mathbf{Q}\downarrow})^T$ with wave vector $\mathbf{Q} = (\pi, \pi)$ becomes

$$\mathcal{H}_{\text{HF}} = \sum_{\mathbf{k}} (\psi^{\dagger}_{\mathbf{k}\sigma} \psi^{\dagger}_{\mathbf{k}+\mathbf{Q}\sigma}) \begin{pmatrix} \hat{h}_{\mathbf{k}} & \sigma \cdot \mathbf{\Delta} \\ \mathbf{\Delta}^{\dagger} \cdot \sigma & \hat{h}_{\mathbf{k}+\mathbf{Q}} \end{pmatrix} \begin{pmatrix} \psi_{\mathbf{k}\sigma} \\ \psi_{\mathbf{k}+\mathbf{Q}\sigma} \end{pmatrix}, \tag{8}$$

where

$$\hat{h}_{\mathbf{k}} = \begin{pmatrix} \epsilon_{\mathbf{k}} & \beta_{\mathbf{k}} - i\gamma_{\mathbf{k}} \\ \beta_{\mathbf{k}} + i\gamma_{\mathbf{k}} & \epsilon_{\mathbf{k}} \end{pmatrix}$$

and

$$\sigma \cdot \mathbf{\Delta} = \begin{pmatrix} \Delta_z & \Delta_x - i\Delta_y \\ \Delta_x + i\Delta_y & -\Delta_z \end{pmatrix}.$$

Here, $\mathbf{\Delta}$ is the exchange field given by $2\mathbf{\Delta} = U\mathbf{m}$, where $\mathbf{m} = m_x \hat{x} + m_y \hat{y} + m_z \hat{z}$ represents the magnetic-moment vector in one of the sublattices. The direction of the magnetic-moment vector will be the opposite in the other sublattice. The twofold-degenerate eigenvalues of the Hamiltonian [Eq. (8)] can be shown to be

$$E_k = \pm \left[\pm 2 \left(\sqrt{\epsilon_k^2 \beta_k^2 + \epsilon_k^2 \gamma_k^2 + \beta_k^2 \Delta_y^2 + \gamma_k^2 \Delta_x^2 - 2\beta_k \gamma_k \Delta_x \Delta_y} \right) + \left(\epsilon_k^2 + \beta_k^2 + \gamma_k^2 + \Delta_x^2 + \Delta_y^2 \right) \right]^{\frac{1}{2}}. \tag{9}$$

The components of the magnetic moments are given in terms of the eigenvectors of the Hamiltonian as follows:

$$m_z = \sum_{\mathbf{k},l}(\phi^*_{\mathbf{k}\uparrow l}\phi_{\mathbf{k}+\mathbf{Q}\uparrow l} - \phi^*_{\mathbf{k}\downarrow l}\phi_{\mathbf{k}+\mathbf{Q}\downarrow l})f(E_{\mathbf{k}l}),$$

$$m_x = \sum_{\mathbf{k},l}(\phi^*_{\mathbf{k}\uparrow l}\phi_{\mathbf{k}+\mathbf{Q}\downarrow l} + \phi_{\mathbf{k}\uparrow l}\phi^*_{\mathbf{k}+\mathbf{Q}\downarrow l})f(E_{\mathbf{k}l}),$$

$$m_y = \sum_{\mathbf{k},l}(-i\phi^*_{\mathbf{k}\uparrow l}\phi_{\mathbf{k}+\mathbf{Q}\downarrow l} + i\phi^*_{\mathbf{k}\uparrow l}\phi_{\mathbf{k}+\mathbf{Q}\downarrow l})f(E_{\mathbf{k}l}), \quad (10)$$

where l is the band index and $f(E)$ is the Fermi-Dirac distribution function.

C. Magnetic susceptibility

In the previous subsection, we discussed only the Hamiltonian for the commensurate AFM order. Whether a commensurate or incommensurate AFM ordered state with in-plane or out-of-plane magnetic moments can be stabilized can be ascertained by examining the static susceptibility given by the 4×4 matrix

$$\hat{\chi}^0(\mathbf{q}) = \begin{pmatrix} \chi^0_{\uparrow\uparrow\uparrow\uparrow}(\mathbf{q}) & \chi^0_{\uparrow\uparrow\uparrow\downarrow}(\mathbf{q}) & \chi^0_{\uparrow\uparrow\downarrow\uparrow}(\mathbf{q}) & \chi^0_{\uparrow\uparrow\downarrow\downarrow}(\mathbf{q}) \\ \chi^0_{\uparrow\uparrow\uparrow\downarrow}(\mathbf{q}) & \chi^0_{\uparrow\uparrow\downarrow\downarrow}(\mathbf{q}) & \chi^0_{\uparrow\uparrow\downarrow\downarrow}(\mathbf{q}) & \chi^0_{\uparrow\downarrow\downarrow\downarrow}(\mathbf{q}) \\ \chi^0_{\downarrow\uparrow\uparrow\uparrow}(\mathbf{q}) & \chi^0_{\downarrow\downarrow\uparrow\uparrow}(\mathbf{q}) & \chi^0_{\downarrow\uparrow\uparrow\downarrow}(\mathbf{q}) & \chi^0_{\downarrow\downarrow\uparrow\downarrow}(\mathbf{q}) \\ \chi^0_{\downarrow\uparrow\uparrow\downarrow}(\mathbf{q}) & \chi^0_{\downarrow\downarrow\uparrow\downarrow}(\mathbf{q}) & \chi^0_{\downarrow\uparrow\downarrow\downarrow}(\mathbf{q}) & \chi^0_{\downarrow\downarrow\downarrow\downarrow}(\mathbf{q}) \end{pmatrix}$$

$$(11)$$

in the presence of SOC [46,47]. A matrix element of the spin susceptibility $\chi^0_{\sigma_1\sigma_2\sigma_3\sigma_4}(\mathbf{q})$ is defined in terms of the two Green's functions in the unordered state as follows:

$$\chi^0_{\sigma_1\sigma_2\sigma_3\sigma_4}(\mathbf{q}) = \sum_{\mathbf{k}} G^0_{\sigma_1\sigma_4}(\mathbf{k})G^0_{\sigma_3\sigma_2}(\mathbf{k}+\mathbf{q}), \quad (12)$$

where

$$G^0(\mathbf{k}) = [-\hat{h}(\mathbf{k})]^{-1}. \quad (13)$$

In the presence of SOC, the directional spin susceptibilities in different directions may be different. Therefore, they can indicate whether magnetic ordering with an in-plane or out-of-plane magnetic moment is preferred. The spin susceptibilities along the three orthogonal directions are χ^0_{xx}, χ^0_{yy}, and χ^0_{zz}, given by

$$\chi^0_{xx}(\mathbf{q}) = \chi^0_{\uparrow\downarrow\uparrow\downarrow}(\mathbf{q}) + \chi^0_{\uparrow\downarrow\downarrow\uparrow}(\mathbf{q}) + \chi^0_{\downarrow\uparrow\uparrow\downarrow}(\mathbf{q}) + \chi^0_{\downarrow\uparrow\downarrow\uparrow}(\mathbf{q}),$$

$$\chi^0_{yy}(\mathbf{q}) = -\chi^0_{\uparrow\downarrow\uparrow\downarrow}(\mathbf{q}) + \chi^0_{\uparrow\downarrow\downarrow\uparrow}(\mathbf{q}) + \chi^0_{\downarrow\uparrow\uparrow\downarrow}(\mathbf{q}) - \chi^0_{\downarrow\uparrow\downarrow\uparrow}(\mathbf{q}),$$

$$\chi^0_{zz}(\mathbf{q}) = \chi^0_{\uparrow\uparrow\uparrow\uparrow}(\mathbf{q}) - \chi^0_{\uparrow\uparrow\downarrow\downarrow}(\mathbf{q}) - \chi^0_{\downarrow\downarrow\uparrow\uparrow}(\mathbf{q}) + \chi^0_{\downarrow\downarrow\downarrow\downarrow}(\mathbf{q}).$$

$$(14)$$

The largest peak for the spin susceptibility $\chi^0_{xx}(\mathbf{q})$ or $\chi^0_{zz}(\mathbf{q})$ occurring at a wave vector $\mathbf{q} = \mathbf{Q}$ implies inherent instability against magnetic ordering with the wave vector $\mathbf{Q}$.

D. Density of states modulation due to a single impurity

Quasiparticle interference is a powerful technique to study low-energy quasiparticle excitations in a system [48]. The

elastic scattering of quasiparticles by an impurity atom generates interference patterns, which may provide important insight, especially into the electronic band structure in the vicinity of the Fermi level. The modulation in the local density of states (DOS) corresponding to the interference patterns can be calculated with the help of a Green's function.

The change induced in the Green's function due to a single impurity with δ potential can be studied by using the t-matrix approximation [49,50]. This change is

$$\delta\hat{G}(\mathbf{k}, \mathbf{k}', \omega) = \hat{G}^0(\mathbf{k}, \omega)\hat{T}(\omega)\hat{G}^0(\mathbf{k}', \omega), \quad (15)$$

where $\hat{G}^0(\mathbf{k}, \omega) = (\omega\hat{I} - \hat{\mathcal{H}}_{\text{HF}})^{-1}$ is the free particle Green's function in an AFM ordered state. The $\hat{T}$ matrix of scattering by an impurity atom is defined in terms of the Green's function given by

$$\hat{T}(\omega) = [\hat{I} - \hat{V}^{\text{imp}}\hat{\mathcal{G}}^0(\omega)]^{-1}\hat{V}^{\text{imp}}, \quad (16)$$

where the Green's function summed over all momenta in the Brillouin zone is

$$\hat{\mathcal{G}}^0(\omega) = \frac{1}{N}\sum_{\mathbf{k}}\hat{G}^0(\mathbf{k}, \omega) \quad (17)$$

and

$$\hat{V}^{\text{imp}}_i = \hat{V}_i \otimes \hat{\sigma}_i,$$

where

$$\hat{V}_i = V_{oi}\begin{pmatrix} 1 & 1 \\ 1 & 1 \end{pmatrix}. \quad (18)$$

$\hat{V}^{\text{imp}}_i$ denotes the 4×4 scattering matrix due to an impurity atom, which is written in terms of Pauli matrices $\sigma_i(i = 1, 2, 3)$ representing various spin-resolved channels of impurity scattering. $i = 0$ corresponds to scattering due to nonmagnetic impurity. We also investigate the behavior of interference patterns generated when the tip of the probe is able to resolve the spin state of the quasiparticle. The spin-resolving tip $\hat{V}^{\text{tip}}$ can be described in terms of Pauli matrices as

$$\hat{V}^{\text{tip}}_i = \hat{V}_i \otimes \hat{\sigma}_i,$$

where

$$\hat{V}_i = V_{ot}\begin{pmatrix} 1 & 1 \\ 1 & 1 \end{pmatrix}. \quad (19)$$

Now, the change $\delta\rho_{ij}(\mathbf{k}, \omega)$ recorded by a spin-resolving tip in the DOS due to the scattering by an impurity atom can be given by [49]

$$\delta\rho_{ij}(\mathbf{q}, \omega) = -\frac{1}{2\pi}\sum_{\mathbf{k}}\text{Im}\big[\text{Tr}\hat{V}^{\text{tip}}_i\hat{G}^0(\mathbf{k}, \omega)\hat{T}(\omega)$$

$$\times \hat{V}^{\text{imp}}_j\hat{G}^0(\mathbf{k}+\mathbf{q}, \omega)\big]. \quad (20)$$

III. RESULTS

A. Magnetic-ordering instability

We begin by examining the magnetic ordering instability in the Rashba-Hubbard model. Figure 1 shows the static magnetic susceptibilities in different directions for the unordered state. Because of the SOC, $SU(2)$ rotational symmetry is
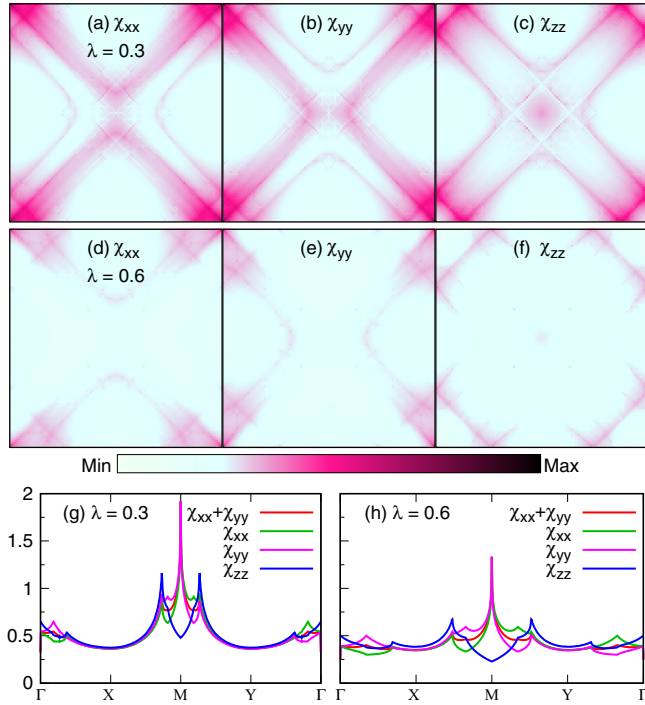
FIG. 1. Various components of the static spin susceptibility (a)–(f) in the whole Brillouin zone and also (g) and (h) along the high-symmetry directions, showing peaks for $\lambda = 0.3$ and 0.6.

absent; therefore, the in-plane component $\chi_{xx}^0(\mathbf{q})$ and the out-of-plane component $\chi_{zz}^0(\mathbf{q})$ are different. Moreover, $\chi_{xx}^0(\mathbf{q})$ and $\chi_{yy}^0(\mathbf{q})$ are also different along high-symmetry directions such as $\Gamma - X$, $\Gamma - Y$, and $M - Y$. We find that both $\chi_{xx}^0(\mathbf{q})$ and $\chi_{yy}^0(\mathbf{q})$ show stronger divergences at (π, π) compared to $\chi_{zz}^0(\mathbf{q})$ when λ is small, implying that the magnetic moments will preferably be oriented in the x-y plane. Second, upon increasing λ, the peak position for $\chi_{zz}^0(\mathbf{q})$ shifts away from (π, π) to an incommensurate wave vector. There is no similar shift in the peak position for the in-plane component of the magnetic susceptibility. The latter is a robust feature in a realistic range for the SOC parameter, which is a result of nesting between the Fermi pockets around the Γ and M points with nesting vector (π, π) (Fig. 2). In the large SOC limit, $t/\lambda \to 0$, we find that χ_{xx} and χ_{yy} are peaked at $(0, \pi)$ and
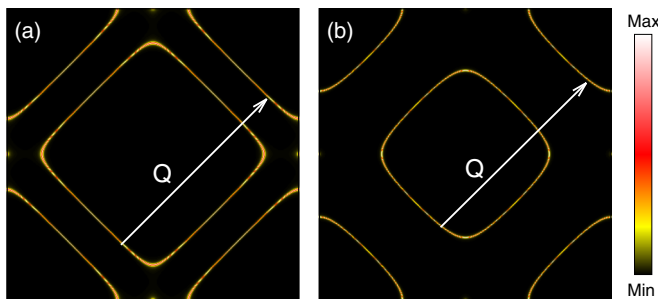

FIG. 2. Fermi surfaces with one of the prominent nesting vectors $\mathbf{Q} = (\pi, \pi)$ at half filling for (a) $\lambda = 0.4$ and (b) $\lambda = 0.8$, where the range of both k_x and k_y is $[-\pi, \pi]$.
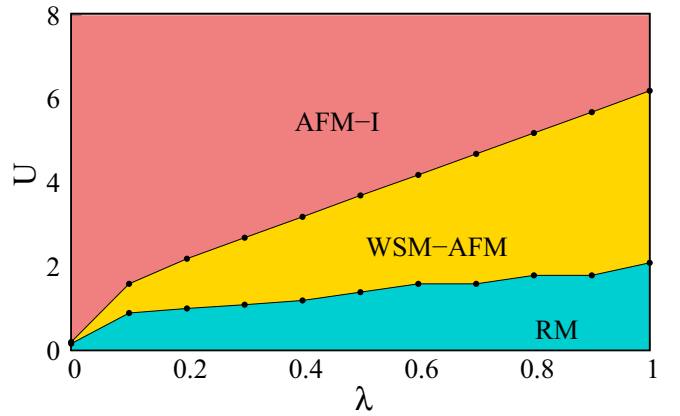

FIG. 3. Phase diagram showing various phases for the correlation strengths $0 \leqslant U \leqslant 8$ and Rashba SOC strength $0 \leqslant \lambda \leqslant 1$. The three different phases are the antiferromagnetic insulator (AFM-I), Weyl semimetallic antiferromagnet (WSM-AFM), and Rashba metal (RM).

$(\pi, 0)$, respectively, whereas χ_{zz} is peaked at $(0, 0)$ instead. Interestingly, all three peaks have the same height, indicating the same strength of instability against ferromagnetic or stripe order. The former set of peaks arises from the interpocket scattering between the pockets around $(0, 0)$ and (π, π). The latter peak originates from the intrapocket scattering. It should be noted that, when $t/\lambda \to 0$, the tiny pockets forming around $(0, 0)$ and (π, π) become Weyl points [45]. Upon inclusion of electron-electron interaction within the random-phase approximation (RPA), the susceptibilities are expected to diverge at the peak positions for a critical value of U and a given λ, indicating a singularity in the free energy and hence the instability of the system against a magnetic order. Our findings thus suggest that the commensurate AFM order with in-plane magnetic moments will be stabilized.

B. WSM-AFM state

Having examined the robustness of the AFM state with in-plane magnetic moment, we now explore the phase diagram in the U-λ parameter space by using the self-consistent mean-field theoretic approach discussed above. Since the in-plane RPA-level magnetic susceptibility is expected to show divergence at the wave vector (π, π), the initial value of the out-of-plane magnetic moment, i.e., m_z, is set to be zero without any loss of generality. Only two types of phases are expected to occur, one with self-consistently obtained magnetic order and another without magnetic order. Throughout the calculations, the inverse temperature parameter ($\beta = 1/kT$) is fixed to be 1000, with k being the Boltzmann constant, which corresponds to ~ 5 K if $t \sim 0.5$ eV.

Figure 3 shows the phase diagram, which consists of phases with magnetic order as well as the Rashba metal (RM) phase without magnetic order. There are two types of magnetically ordered states. One is the AFM insulator (AFM-I) occurring for higher U, and the other is the topological WSM state with magnetic order (WSM-AFM) existing for relatively lower values of U, which will be discussed at length later because it is the main focus of the current work. In an earlier
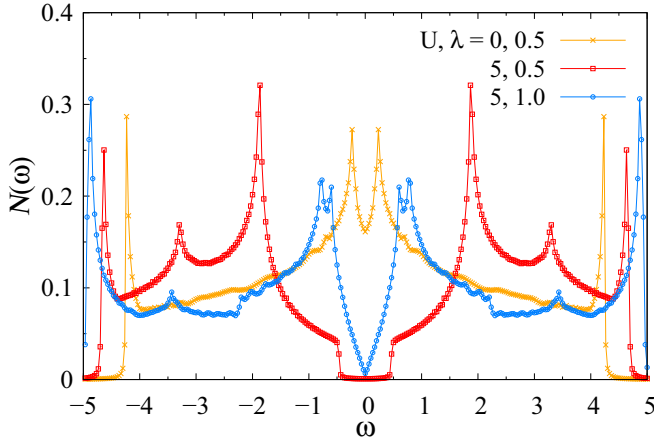
FIG. 4. DOS corresponding to the three different phases, RM, AFM-I, and WSM-AFM. For $U = 0$ and $\lambda = 0.5$, a significant DOS is obtained at the Fermi level characteristic of a metallic system. In the case of $U = 5$ and $\lambda = 0.5$, the DOS is gapped at the Fermi level, indicating the insulating behavior of the system. Upon increasing SOC further so that $\lambda = 1$, the DOS is zero at the Fermi level, whereas it does not vanish in the immediate vicinity, indicating a semimetallic state.

work [38], a pseudogaplike phase with AFM order was reported based on the finding of a dip in the DOS (Fig. 4), which is similar to the one observed in the so-called pseudogap phases found in hole-doped cuprates [51,52]. However, the dispersion plotted in various high-symmetry directions $(0, 0) \rightarrow (\pi, \pi) \rightarrow (0, \pi) \rightarrow (-\pi/2, \pi/2)$ provides a hint about the topological nature of this magnetically ordered state because two pairs of linear nondegenerate band crossings at the Fermi level exist, giving rise to two pairs of symmetry-protected Weyl points (Figs. 5 and 6).
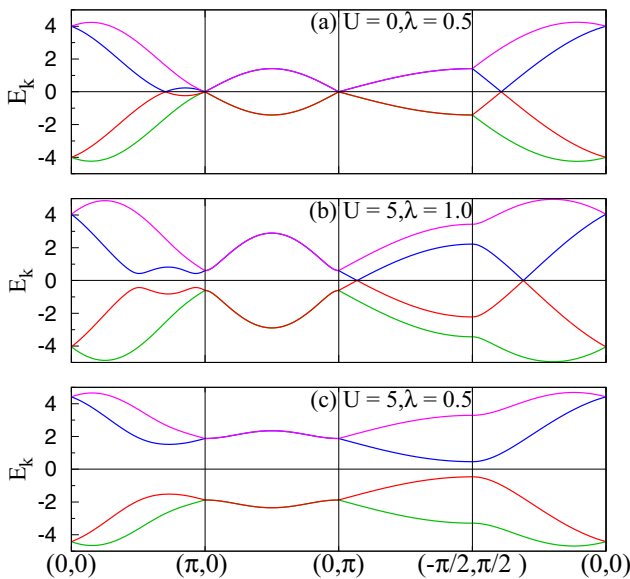

FIG. 5. Electronic dispersions are plotted for different sets of U and λ values. They correspond to the three phases: (a) RM, (b) WSM-AFM, and (c) AFM-I.
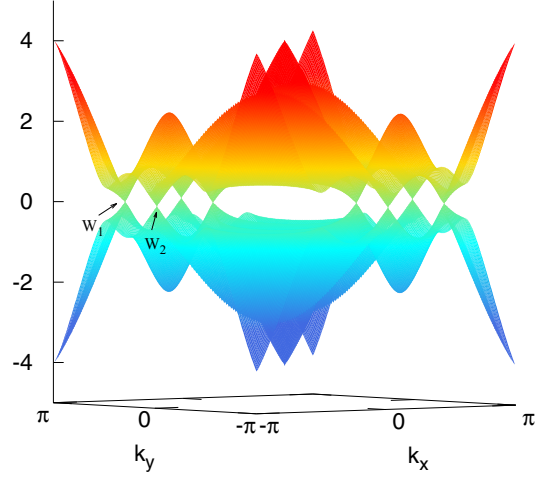

FIG. 6. Electronic dispersion in the WSM-AFM shown for the entire Brillouin zone.

The Hamiltonian $\mathcal{H}_{\mathrm{HF}}$ lacks both the time-reversal invariance ($\mathcal{T}$) and inversion ($\mathcal{P}$) symmetries, when considered independently. In order to see this, we rewrite the mean-field Hamiltonian in the sublattice basis formed because of AFM ordering as

$$\mathcal{H}_{\mathrm{HF}} = \epsilon_{\mathbf{k}}\sigma_0 \otimes \tau_1 + \Delta_x \sigma_1 \otimes \tau_0 + \Delta_y \sigma_2 \otimes \tau_0$$
$$+ 2\lambda \sin k_y \sigma_1 \otimes \tau_1 - 2\lambda \sin k_x \sigma_2 \otimes \tau_1. \quad (21)$$

Here, σ_i and τ_j are the Pauli matrices used for the spin and sublattice degrees of freedom. It should be noted that only a few of the five matrices formed by σ_i and τ_j in the Hamiltonian anticommute; i.e., they do not form Dirac algebra.

None of the terms in the Hamiltonian commute even for $\Delta_x = \Delta_y = 0$, i.e., when the AFM order is absent. In that case, along $\pm k_x \mp k_y = \pi$, the first term's contribution vanishes, and the remaining two terms anticommute. Then, the Hamiltonian has both time-reversal ($\mathcal{T} = i\sigma_2 K$) and inversion ($\mathcal{P} = \tau_1$) symmetries, which leads to the twofold-degenerate bands along $(0, \pi) \rightarrow (-\pi/2, \pi/2)$ and Dirac points (DPs) at $(0, \pi)$ and $(\pi, 0)$. This is mainly the consequence of Brillouin zone folding. In the absence of magnetic ordering, the folding is not required; then the degeneracy disappears, and the DPs change into the WPs. The degeneracy of the bands is lifted, and the DPs are split into WPs if the system develops nonzero magnetic moment. One of the WPs is shifted away from $(0, \pi)$ along $(0, \pi) \rightarrow (-\pi/2, \pi/2)$. Another band degeneracy occurs along $(\pi, 0) \rightarrow (0, \pi)$, i.e., along $k_x + k_y = \pi$, which persists even in the AFM ordered state. This is a consequence of the fact that the first term vanishes while the rest anticommute with each other.

With magnetic order, both the time-reversal and inversion symmetries are broken. It is not difficult to see that the second and third terms break the time-reversal symmetry, while the fourth and fifth terms are responsible for the absence of inversion symmetry. However, the Hamiltonian is invariant under the combined operation defined by $\mathcal{TP}$, i.e., $\mathcal{TP}(\mathcal{H}_{\mathrm{HF}}(\mathbf{k}))(\mathcal{TP})^{-1} \rightarrow \mathcal{H}_{\mathrm{HF}}(\mathbf{k})$. Unlike the system considered here without inversion symmetry, earlier works show that stable DPs can be obtained in the nonsymmorphic system

with second-neighbor SOC in the absence of time-reversal and inversion symmetries while both combinedly remain intact [53].

The bands crossing at the Fermi level in the WSM-AFM state disappears with a rise in the value of U. The boundary between the AFM-I and WSM-AFM states is determined by the condition $|\Delta| \leqslant 2\lambda$, which should be satisfied by the magnetic exchange coupling Δ. On lowering U further, there is a phase transition from WSM-AFM to RM, with the magnetic moment vanishing to zero in the self-consistent scheme. This happens because the spin susceptibility does not diverge at **Q** for a given set of parameters, which includes on-site Coulomb interaction. In the following, we find the condition satisfied by the magnetic order parameter to determine whether the AFM ordered state is Weyl semimetallic or not. First of all, we note that the self-consistently obtained in-plane magnetization has the same magnitude along both directions, i.e., $\Delta_x = \Delta_y = \Delta$. If the condition $|\Delta| \leqslant 2\lambda$ is satisfied, then one pair of WPs (W_1) is located along the $k_x - k_y = \pi$ and $-k_x + k_y = \pi$ directions, whereas the other pair (W_2) is located along $k_x = -k_y$, as seen in Fig. 5. Note that the word "pair" does not necessarily mean that they have opposite winding numbers, which will be discussed later; it is used here only to indicate their location in the Brillouin zone.

C. WPs along $\pm k_x \mp k_y = \pi$

For the pair of Weyl points W_1 located along $k_x - k_y = \pi$ and $-k_x + k_y = \pi$ (Fig. 5), $\epsilon_\mathbf{k} = 0$, and $\beta_\mathbf{k} = -\gamma_\mathbf{k}$. Therefore, the eigenvalues [Eq. (9)] of the Hamiltonian matrix in the magnetically ordered state reduce to

$$E_{1\mathbf{k}} = \pm\sqrt{2(\beta_\mathbf{k} - \Delta)^2}. \tag{22}$$

As the dispersion near WPs [say, (k_{x_o}, k_{y_o})] is linear, Taylor-series expansion around these points by replacing $k_x' \rightarrow k_{x_o} + q_x$ and $k_y' \rightarrow k_{y_o} + q_y$ with small $\mathbf{q}$ gives

$$E_{1\mathbf{q}} = \pm\sqrt{2}[2\lambda(\sin k_{y_o} + q_y \cos k_{y_o}) - \Delta]. \tag{23}$$

The dispersion can be linear, and the band crossing will appear at (k_{x_o}, k_{y_o}), provided $2\lambda \sin k_{y_o} = \Delta$. In that case

$$E_{1\mathbf{q}} = \pm c q_y, \tag{24}$$

where c is a constant term given by $c = 2\sqrt{2}\lambda[\sqrt{1 - (\frac{\Delta}{2\lambda})^2}]$. Since $|\sin k_{y_o}| \leqslant 1$, a linearized dispersion will be obtained at $k_{y_o} = \sin^{-1}\frac{\Delta}{2\lambda}$ whenever the self-consistently computed exchange field satisfies the condition $|\Delta| \leqslant 2\lambda$.

D. WPs along $k_x = -k_y$

Next, we examine the linear-band crossing for the other pair of WPs, W_2, which is found along $k_x = -k_y$. Along this direction, $\beta_\mathbf{k} = -\gamma_\mathbf{k}$, and $\epsilon_\mathbf{k} = -4t \cos k_y$. Therefore, the energy eigenvalues reduce to

$$E_{2\mathbf{q}} = \pm[\sqrt{(-4t \cos k_y)^2 + 2\Delta^2} - \sqrt{2}\beta_\mathbf{k}]. \tag{25}$$

Now introducing the Taylor-series expansion around the momenta corresponding to $W_2 = (k_{x_o}, k_{y_o})$, we obtain the linearized dispersion

$$E_{2\mathbf{q}} = \pm c' q_y, \tag{26}$$

where

$$c' = \left(\frac{16t^2 b'}{\sqrt{b}} + 2\sqrt{2}\lambda\right)(\sqrt{1 - b'^2}) \tag{27}$$

and

$$b = (4t\sqrt{1 - b'^2})^2 + 2\Delta^2. \tag{28}$$

The linearized dispersion and WPs are possible only when $|b'| \leqslant 1$, where

$$b' = \sin k_{y_o} = \sqrt{\frac{8t^2 + \Delta^2}{4\lambda^2 + 8t^2}}. \tag{29}$$

This again yields the condition $|\Delta| \leqslant 2\lambda$, the same as in the case of W_1 points. The location of W_2 can be obtained with the help of Eq. (29) by calculating k_{y_o}.

E. Chern numbers for WPs W_1 and W_2

In the previous subsections, we focused on the linearized dispersion in the vicinity of WPs W_1 and W_2. Next, we address the question of winding numbers associated with these WPs. In the unordered state, the WPs occurring at $(0, 0)$ and $(\pi, 0)$ have winding numbers 1 and -1, respectively. However, in the magnetic Brillouin zone, the calculation of winding numbers using Eq. (9) analytically may be a difficult task; therefore, we adopt a numerical approach. The winding number for the pair of WPs W_1 and W_2 can be obtained by calculating the following line integral [54]:

$$w = -\frac{i}{2\pi} \oint \mathbf{A}^{(n)}(\mathbf{k}) \cdot d\mathbf{l}, \tag{30}$$

performed along a closed contour enclosing a WP, where the Berry connection $\mathbf{A}^{(n)}(\mathbf{k})$ for the nth band is given by

$$A_i^{(n)}(\mathbf{k}) = \langle u_n(\mathbf{k})|\frac{\partial}{\partial k_i}|u_n(\mathbf{k})\rangle. \tag{31}$$

$|u_n(\mathbf{k})\rangle$ is the eigenvector of the Hamiltonian given by Eq. (8). The calculation using Eq. (29) yields the winding number w for WPs W_1 and W_2 along $\pm k_x \mp k_y = \pi$ and $k_x = -k_y$, 1 and -1, respectively. Figure 7 shows the vector field associated with the Berry connection in the entire Brillouin zone, and a zoomed-in view of two such points with counterclockwise and clockwise rotation is presented in Fig. 8.

F. Edge states

As discussed above, WPs exist inside and on the boundary of the reduced Brillouin zone with winding numbers ± 1. Therefore, the existence of edge states along a quasi-one-dimensional chain is guaranteed in a way similar to the case of graphene [55,56] or other magnetically ordered systems with Dirac points [53,57]. These edge states, in the case of topological insulators, are pairs of states propagating in directions opposite to each other. The edge state dispersion crosses the Fermi level and connects the valence and conduction bands. In order to explore the edge state in the WSM-AFM state, we consider a ribbon oriented along the x direction consisting of N chains of atoms positioned along the y direction such that k_x becomes a good quantum number. Thus, the Hamiltonian
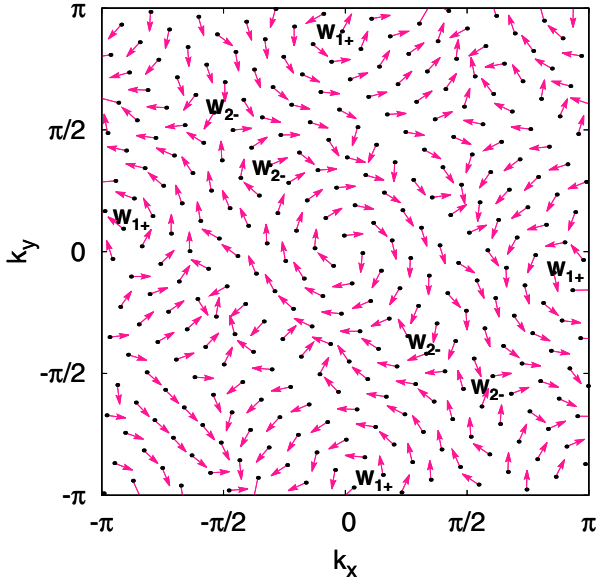
FIG. 7. Berry connection $A(\mathbf{k})$ plotted for the whole Brillouin zone. The nature of winding about each WP is denoted by either W_+ or W_-, where positive and negative signs indicate counterclockwise and clockwise windings, respectively.

H_{Rbx} for the ribbon is a $4N \times 4N$ matrix given by

$$H_{Rbx}(\mathbf{k}) = \begin{pmatrix} H_1^+ & H_2 & O & H_3 & \cdots \\ H_2^\dagger & H_1^- & H_3 & O & \cdots \\ O & H_3^\dagger & H_1^+ & H_2 & \cdots \\ H_3^\dagger & O & H_2^\dagger & H_1^- & \cdots \\ \vdots & \vdots & \vdots & \vdots & \ddots \end{pmatrix}, \quad (32)$$

where

$$H_1^\pm = \begin{pmatrix} 0 & \pm(\Delta_x - i\Delta_y) \\ \pm(\Delta_x + i\Delta_y) & 0 \end{pmatrix},$$

$$H_2 = \begin{pmatrix} 2t\cos k_x & 2i\lambda\sin k_x \\ -2i\lambda\sin k_x & 2t\cos k_x \end{pmatrix},$$
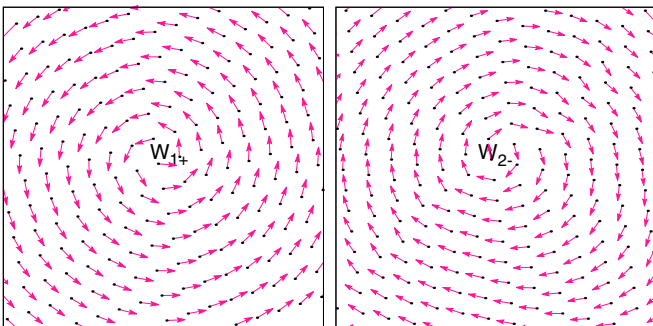

FIG. 8. Zoomed-in view of the Berry connection about the Weyl points shown in Fig. 7 because the rotation of the fields is not clear, especially in the case of W_{2-}.
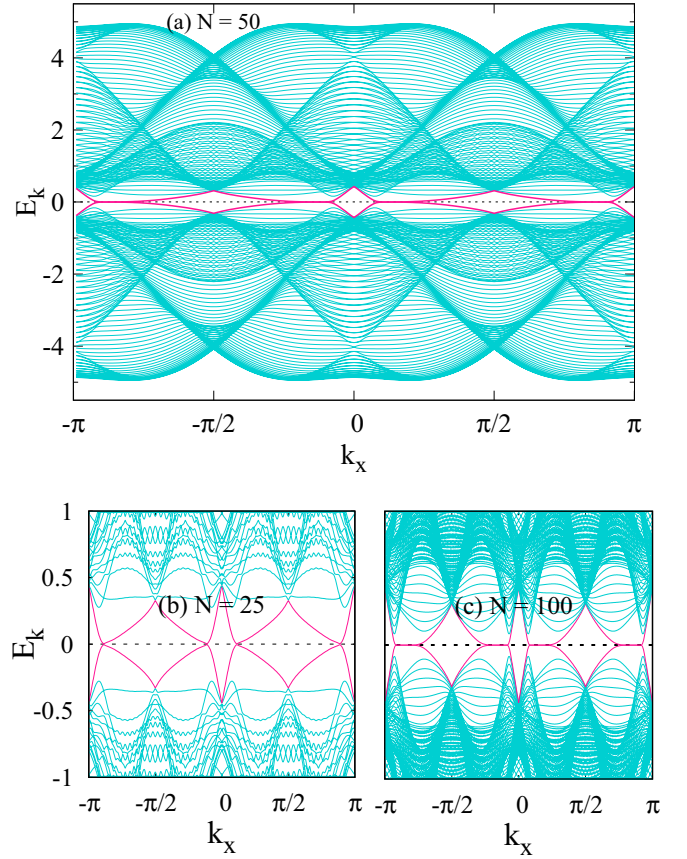

FIG. 9. For the set of parameters $U = 5$ and $\lambda = 1$, (a) the edge state and bulk band dispersions are plotted for a ribbon of width $N = 50$ extended along the x direction and projected onto a one-dimensional Brillouin zone. The edge states crossing the band gap are colored differently for clarity. Also shown are zoomed-in versions for different sizes: (b) $N = 25$ and (c) $N = 100$.

and

$$H_3 = \begin{pmatrix} t & i\lambda \\ i\lambda & t \end{pmatrix}.$$

In Fig. 9, the bands crossing the Fermi energy shown in different colors correspond to the edge states. Above and below are the bulk dispersion bands, which are gapped. The edge states cross the Fermi level at four different points; two of the crossings lie very close to $-\pi$ and π, while the other two lie near $k_x = 0$. We find that the crossing turns into a flat degenerate band as the number of chains in the ribbon is increased. Here, we focus on a ribbon oriented along the x direction. When the ribbon is oriented along the y direction, the same edge state dispersion is obtained, which is a consequence of the reflection symmetry about the line $k_x = k_y$ in the Brillouin zone. Although we have restricted our calculations to the direction along the primitive translational vectors of the original lattice, it would be interesting to study the edge states when the ribbons are oriented along the primitive translational vector of the reduced Brillouin zone, when the chains consist of sites belonging to only a particular sublattice, i.e., the magnetic moments are aligned along the same direction.
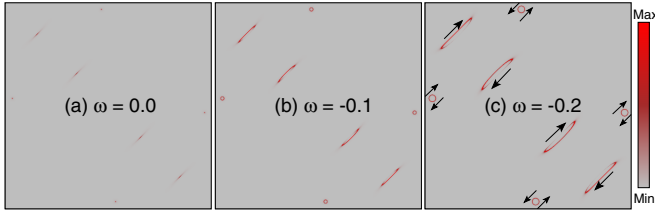
FIG. 10. Constant-energy contours (CECs) obtained in the WSM-AFM state for energies (a) $\omega = 0.0$, (b) $\omega = -0.1$, and (c) $\omega = -0.2$. The arrows in (c) indicate orientation of spin along the CECs.

G. Quasiparticle interference

A conclusive signature of Weyl points may be obtained with the help of spin- and angle-resolved photoemission spectroscopy [58]. In addition, the scanning-tunneling microscopy (STM), which can detect the impurity-generated modulation in the local density of states, i.e., QPI, can be another effective tool to confirm Weyl points.

The QPI pattern for a nontopological system is determined primarily by the spectral-density distribution along the constant-energy contours (CECs) for a given energy as well as by the shape of the contours [59]. In particular, the patterns are dominated by those scattering vectors which connect the regions with high spectral density [60]. However, the situation is contrastingly different for a helical Fermi liquid in topological semimetals, where the backscattering by a nonmagnetic impurity atom may not be allowed; therefore, no characteristic response is expected in the patterns. On the other hand, the magnetic impurity generates only a weak response [49]. If the tip of the probe can differentiate the spin state of the quasiparticle, the QPI patterns can provide crucial information about the band structure in the vicinity of the Fermi surface as well as the spin texture. Here, in the WSM-AFM, only two species of quasiparticles exist, with spin oriented either along $\hat{x} + \hat{y}$ or along $-\hat{x} - \hat{y}$, where $\hat{x}$ and $\hat{y}$ are the unit vectors directed along the primitive translational vectors. The orientation of the quasiparticle spin is in accordance with the direction of the magnetic moments in the WSM-AFM state.

Figures 10(a) and 10(b) show CECs for $\omega = -0.1$ and -0.2. There are two types of CECs in the magnetic Brillouin zone. One has a circular shape, which has spins pointing along $\hat{x} + \hat{y}$ in one half and along $-\hat{x} - \hat{y}$ in the other half. The quasiparticle spin is required to change direction abruptly at the intersection of a circular CEC and a line running along the zone-diagonal direction and bisecting the CEC. The other set of CECs looks like the cross section of a banana along its length, with highly nonuniform spectral density. It should be noted that each of these CECs in the magnetic Brillouin zone has a quasiparticle with spin pointing along only one direction. In other words, upon moving along the CECs and completing one cycle, there is no change in the spin direction. Thus, the orientation of the quasiparticle spin changes along CECs, which is different from the way it changes along the cross section of a Dirac cone in a helical liquid existing on the surface of a strong topological insulator [49].
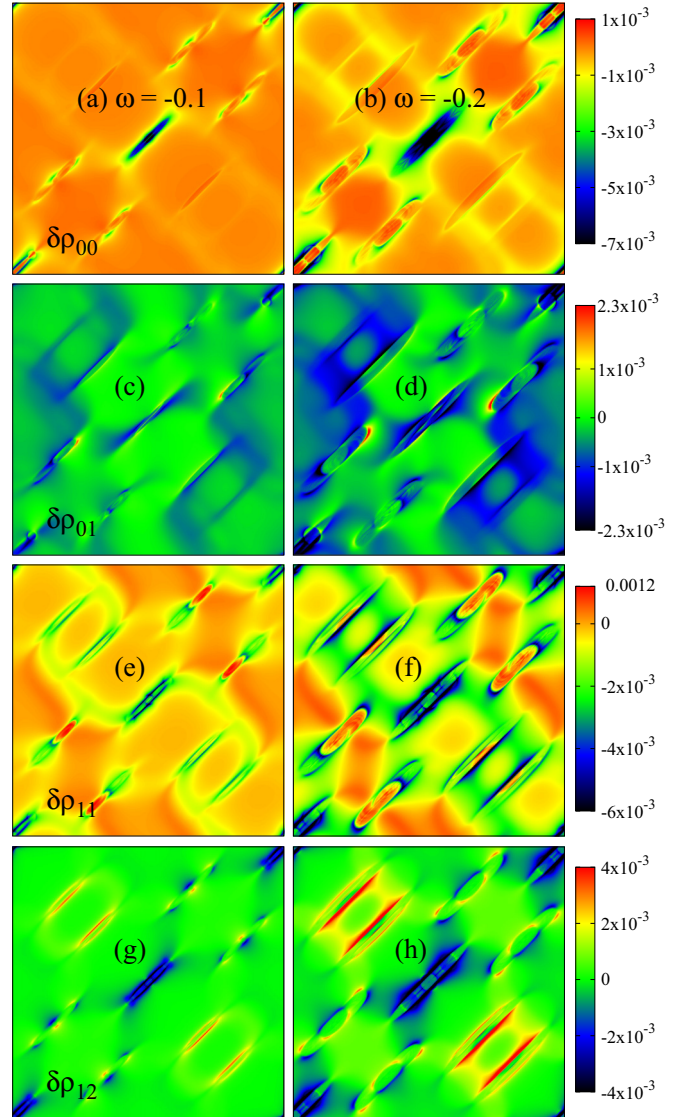

FIG. 11. QPI patterns due to nonmagnetic impurity ρ_{00} (first row) and magnetic impurity ρ_{01} (second row). The third and fourth rows show the QPI patterns ρ_{11} and ρ_{12} detected by the spin-state-sensitive tip due to a magnetic impurity. The first column corresponds to energy $\omega = -0.1$, while the second column corresponds to $\omega = -0.2$.

Unlike the Dirac cone generated QPI patterns, in which the nonmagnetic impurities can give rise to only weak and nonsingular response [61], the patterns in the WSM-AFM state are not featureless. Figure 11 shows the QPI patterns obtained for $V_{oi} = 0.1$ and $V_{ot} = 0.1$. The main reason for obtaining such patterns is only two possible orientations of electronic spin along the CECs. The intrapocket scattering of the banana-shaped CECs generates a pattern with a similar shape at Γ because the quasiparticle spin has the same orientation everywhere. The pattern at Γ also has an intrapocket contribution due to the circular pockets near points like $(\pi, 0)$, which is weak and unnoticeable because of tiny scattering vectors. The patterns at $(\pm\pi, \mp\pi)$ are generated by the interpocket scattering between the banana-shaped CECs belonging to the reduced Brillouin zone and the one outside it, separated

by $(\pm\pi, \mp\pi)$ in momentum space. It should be noted that they have the same orientation of the spin. On the other hand, the interpocket scattering between the two banana-shaped CECs belonging to the reduced Brillouin zone does not generate any pattern because of opposite spin orientation. The interpocket scattering between the circular and banana-shaped pockets also creates a noticeable pattern because one side of the circular pocket has the quasiparticle spin aligned along the spin of the quasiparticle associated with the banana-shaped CECs.

The second row in Fig. 11 shows ρ_{01}, the patterns generated by the magnetic impurity with spin along the x direction when the STM is spin insensitive. The pattern generated by the intrapocket scattering from the banana-shaped CECs appears to be weak. More or less similar behavior is observed for the patterns originating from the interpocket scattering. The weak patterns originate because the quasiparticle spin direction is flipped after impurity scattering. Further, the scattered quasiparticle has a reduced DOS with spin oriented along the positive x direction. Note that this is also true for the quasiparticle with the spin component along the negative x direction. On the other hand, the spin-resolved QPI shows strong patterns, which arise because of the specific orientation of the quasiparticle spin after scattering and are then detected by the spin-sensitive STM probe. ρ_{11} patterns show strong singular features resulting from both the intrapocket and interpocket scatterings. The intrapocket scattering leads to two linear patterns around Γ as well as around $\pm(\pi, \pm\pi)$. The interpocket scattering between the two nearest banana-shaped CECs results in two linear patterns around $(\pm\pi/2, \mp\pi/2)$. The orientation of the pattern follows directly from the alignment of CECs. QPI patterns resulting from the interpocket scattering between the circular and banana-shaped CECs are also easily noticeable. These features are more or less repeated for ρ_{12} when the impurity spin is oriented along the y direction while the STM probe has spin oriented along the x direction. The similarity results from the fact that the quasiparticle spins are not oriented along the x or y direction but instead along $x + y$ or $-x - y$.

IV. DISCUSSION

The search for symmetry-protected two-dimensional topological semimetals similar to graphene has significant theoretical interest as well as technological applications. These topological semimetals may be protected by the crystalline symmetries and can be destroyed by magnetic ordering as the time-reversal symmetry is broken [62,63]. However, some recent studies indicated that the magnetic order can coexist with a topological semimetallic state. For instance, the DPs were observed in the SDW state of iron pnictides [64]. These DPs are protected by the collinearity of the SDW state, inversion symmetry about an iron atom, and invariance under the combined time-reversal and inversion symmetry of magnetic moments [65]. Similarly, a Dirac-semimetallic state was predicted to exist in a system with nonsymmorphic symmetry when both $\mathcal{T}$ and $\mathcal{P}$ are broken [53,66]. In this current work, we have demonstrated the existence of a WSM state with AFM order with a checkerboard arrangement of spins within the Rashba-Hubbard model, where the

time-reversal and inversion symmetries are both individually absent. However, the combined time-reversal and inversion symmetry is protected even in the absence of nonsymmorphic symmetries.

In the current work, the phase diagram is obtained at a temperature $T = 0.001$ in units of t. This particular value of temperature corresponds to ~ 5 K if t is taken to be ~ 500 meV. With the rise in the temperature, the magnetic moments can melt away within the static mean-field theory, or randomness can be introduced in their orientation if more sophisticated approaches involving Monte Carlo simulations based on auxiliary-field methods are used [67,68]. For this reason, the AFM order makes room for the RM phase in the phase diagram. A similar phase diagram without the WSM-AFM state was reported previously at a very low temperature, where the difference between the free-energy and ground state energy becomes increasingly small [38]. It is worth noting that when $T \to 0$ K, the Rashba metallic state will not be found at all. Therefore, the area occupied by the WSM-AFM state will increase with decreasing temperature. Second, with a rise in temperature, as the magnetic moments melt away, W_1 will be shifted to the point $(\pi, 0)$, whereas W_2 will move toward the momentum with $k_{y_o} = \sin^{-1}\left(\frac{8t^2}{4\lambda^2 + 8t^2}\right)$. A similar effect on the phase diagram is expected when the quantum correction to the sublattice magnetization is incorporated, which will reduce the sublattice magnetization [69]. The current approach ignores the spatial and thermal fluctuations in the magnetic moments. It is of strong interest to see the consequences of such fluctuations on the stability of the WSM state, which can be studied most effectively with the exact diagonalization plus Monte Carlo approach [67,68].

In addition to the Hartree-Fock mean-field theory, the U-λ phase diagram was obtained via VMC [39]. However, the WSM is found for larger λ when the Fermi surface shrinks to a point at the high-symmetry points $(0, 0)$ and (π, π). Such a Fermi surface structure is unlikely to lead to robust magnetic ordering, and therefore, the corresponding WSM state may exist without any magnetic order. Second, the WSM state sandwiched between the Rashba metal and AFM insulator does not occur for a low value of λ. Our calculations, on the other hand, demonstrate that if the magnetic moments in the AFM ordered state satisfy the condition $|\Delta| \leqslant 2\lambda$, then the AFM ordered state can coexist with the WSM state. Therefore, in future studies, it would be interesting to determine what kind of band structure will be supported for the AFM insulating state obtained via the VMC method when the condition $|\Delta| \leqslant 2\lambda$ is fulfilled.

Here, we have restricted our effort to half filling with a focus on the previously reported metallic antiferromagnetic state with pseudogaplike features in the density of states [38]. It would be interesting in future work to examine the possible existence of topological states with incommensurate magnetic order stabilized away from half filling. Moreover, our calculation shows that the second-neighbor hopping can also support the Weyl points but not necessarily a Weyl semimetallic state. This is because the pairs of Weyl points are shifted away from the Fermi level in opposite directions. It may appear that the band filling can be changed in order to force one of the Weyl points to lie at the Fermi level. However, it will be accompanied by additional

bands crossing the Fermi level. In addition, the nature of magnetic order may not necessarily remain the checkerboard type.

V. CONCLUSION

In conclusion, we showed the existence of Weyl semimetallic states with antiferromagnetic order in the Rashba-Hubbard model in a realistic range of interaction and spin-orbit coupling parameters. The Weyl semimetallic state is accompanied by two pairs of Weyl points inside the reduced Brillouin zone, where the combination of both inversion and time-reversal symmetries exists when they are taken together, although both symmetries are absent individually because of the Rashba spin-orbit coupling and magnetic order. In addition, the linear dispersion in the vicinity of Weyl points, winding numbers, and associated edge state dispersion were also studied. Finally, both spin-sensitive and spin-insensitive quasiparticle interferences were investigated, which provided valuable insight into the nature of quasiparticle spin states in the vicinity of the Weyl points.

ACKNOWLEDGMENTS

[1] P. W. Anderson, *Basic Notions of Condensed Matter Physics* (Westview Press, Boulder, CO, 1997).

[2] K. v. Klitzing, G. Dorda, and M. Pepper, New method for high-accuracy determination of the fine-structure constant based on quantized Hall resistance, Phys. Rev. Lett. **45**, 494 (1980).

[3] B. A. Bernevig and S. C. Zhang, Quantum spin Hall effect, Phys. Rev. Lett. **96**, 106802 (2006).

[4] L. Fu, C. L. Kane, and E. J. Mele, Topological insulators in three dimensions, Phys. Rev. Lett. **98**, 106803 (2007).

[5] D. Hsieh, D. Qian, L. Wray, Y. Xia, Y. S. Hor, R. J. Cava, and M. Z. Hasan, A topological Dirac insulator in a quantum spin Hall phase, Nature (London) **452**, 970 (2008).

[6] M. König, S. Wiedmann, C. Brüne, A. Roth, H. Buhmann, L. Molenkamp, X.-L. Qi, and S.-C. Zhang, Quantum spin Hall insulator state in HgTe quantum wells, Science **318**, 766 (2007).

[7] Y. Xia, L. Wray, D. Qian, D. Hsieh, A. Pal, H. Lin, A. Bansil, D. Grauer, Y. Hor, R. Cava, and M. Hasan, Observation of a large-gap topological-insulator class with a single Dirac cone on the surface, Nat. Phys. **5**, 398 (2009).

[8] H. Zhang, C.-X. Liu, X.-L. Qi, X. Dai, Z. Fang, and S.-C. Zhang, Topological insulators in Bi_2Se_3, Bi_2Te_3 and Sb_2Te_3 with a single Dirac cone on the surface, Nat. Phys. **5**, 438 (2009).

[9] X.-L. Qi and S.-C. Zhang, Topological insulators and superconductors, Rev. Mod. Phys. **83**, 1057 (2011).

[10] R. Winkler, *Spin-Orbit Coupling Effects in Two-Dimensional Electron and Hole Systems* (Springer, Berlin, 2003).

[11] A. A. Abrikosov and L. P. Gor'kov, Spin-orbit interaction and the Knight shift in superconductors, Sov. Phys. JETP **15**, 752 (1962).

[12] E. Orlenko, E. Sheka, and F. Orlenko, Influence of spin-orbit interaction on magnetic properties of fullerenes, Eur. Phys. J. D **70**, 59 (2016).

[13] E. C. Gingrich, B. M. Niedzielski, J. A. Glick, Y. Wang, D. L. Miller, R. Loloee, W. P. Pratt, Jr., and N. O. Birge, Controllable $0–\pi$ Josephson junctions containing a ferromagnetic spin valve, Nat. Phys. **12**, 564 (2016).

[14] Z.-P. Niu, A spin triplet supercurrent in half metal ferromagnet/superconductor junctions with the interfacial Rashba spin-orbit coupling, Appl. Phys. Lett. **101**, 062601 (2012).

[15] J. Linder and J. W. A. Robinson, Superconducting spintronics, Nat. Phys. **11**, 307 (2015).

[16] A. Ptok, K. Rodríguez, and K. J. Kapcia, Superconducting monolayer deposited on substrate: Effects of the spin-orbit coupling induced by proximity effects, Phys. Rev. Mater. **2**, 024801 (2018).

[17] J. Alicea, New directions in the pursuit of Majorana fermions in solid state systems, Rep. Prog. Phys. **75**, 076501 (2012).

[18] C. W. J. Beenakker, Search for Majorana fermions in superconductors, Annu. Rev. Condens. Matter Phys. **4**, 113 (2013).

[19] S. R. Elliott and M. Franz, Colloquium: Majorana fermions in nuclear, particle, and solid-state physics, Rev. Mod. Phys. **87**, 137 (2015).

[20] L. Fu and C. L. Kane, Superconducting proximity effect and Majorana fermions at the surface of a topological insulator, Phys. Rev. Lett. **100**, 096407 (2008).

[21] S. Tewari, S. Das Sarma, Ch. Nayak, Ch. Zhang, and P. Zoller, Quantum computation using vortices and Majorana zero modes of a $p_x + ip_y$ superfluid of fermionic cold atoms, Phys. Rev. Lett. **98**, 010506 (2007).

[22] E. I. Rashba, Properties of semiconductors with an extremum loop. I. Cyclotron and combinational resonance in a magnetic field perpendicular to the plane of the loop, Sov. Phys. Solid State **2**, 1109 (1960).

[23] Y. A. Bychkov and E. I. Rashba, Oscillatory effects and the magnetic susceptibility of carriers in inversion layers, J. Phys. C **17**, 6039 (1984).

[24] V. I. Sheka and E. I. Rashba, Properties of semiconductors with an extremum loop. IV. Angular dependence of combination resonance in a strong magnetic field, Sov. Phys. Solid State **3**, 1718 (1962).

[25] E. I. Rashba and V. I. Sheka, Combined resonance in electron InSb, Sov. Phys. Solid State **3**, 1357 (1961).

[26] J. Nitta, T. Akazaki, H. Takayanagi, and T. Enoki, Gate control of spin-orbit interaction in an inverted $In_{0.53}Ga_{0.47}As/In_{0.52}Al_{0.48}As$ heterostructure, Phys. Rev. Lett. **78**, 1335 (1997).

[27] T. Schäpers, G. Engels, J. Lange, T. Klocke, M. Hollfelder, and H. Luth, Effect of the heterointerface on the spin splitting in modulation doped $In_xGa_{1-x}As/InP$ quantum wells for $B \rightarrow 0$, J. Appl. Phys. **83**, 4324 (1998).

[28] S. Bandyopadhyay and M. Cahay, Reexamination of some spintronic field-effect device concepts, Appl. Phys. Lett. **85**, 1433 (2004).

[29] T. Jungwirth, J. Wunderlich, and K. Olejník, Spin Hall effect devices, Nat. Mater. **11**, 382 (2012).

[30] A. Manchon, H. C. Koo, J. Nitta, S. M. Frolov, and R. A. Duine, New perspectives for Rashba spin-orbit coupling, Nat. Mater. **14**, 871 (2015).

[31] C. Chappert, A. Fert, and F. N. Van Dau, The emergence of spin electronics in data storage, Nat. Mater. **6**, 813 (2007).

[32] E. Knill, Quantum computing with realistically noisy devices, Nature (London) **434**, 39 (2005).

[33] W. Witczak-Krempa, G. Chen, Y. B. Kim, and L. Balents, Correlated quantum phenomena in the strong spin-orbit regime, Annu. Rev. Condens. Matter Phys. **5**, 57 (2014).

[34] J. Beyer, J. B. Profe, L. Klebl, T. Schwemmer, D. M. Kennes, R. Thomale, C. Honerkamp, and S. Rachel, Rashba spin-orbit coupling in the square-lattice Hubbard model: A truncated-unity functional renormalization group study, Phys. Rev. B **107**, 125115 (2023).

[35] D. Bercioux and P. Lucignano, Quantum transport in Rashba spin-orbit materials: A review, Rep. Prog. Phys. **78**, 106001 (2015).

[36] J. Bertinshaw, Y. K. Kim, G. Khaliullin, and B. J. Kim, Square lattice iridates, Annu. Rev. Condens. Matter Phys. **10**, 315 (2019).

[37] K. Kubo, Enhanced spin-orbit coupling in a correlated metal, J. Phys. Soc. Jpn. **91**, 124707 (2022).

[38] W. Kennedy, S. dos Anjos Sousa-Júnior, N. C. Costa, and R. R. dos Santos, Magnetism and metal-insulator transitions in the Rashba-Hubbard model, Phys. Rev. B **106**, 165121 (2022).

[39] K. Kubo, Weyl semimetallic state in the Rashba–Hubbard model, J. Phys. Soc. Jpn. **93**, 024708 (2024).

[40] X. Zhang, W. Wu, G. Li, L. Wen, Q. Sun, and A. Ji, Phase diagram of interacting Fermi gas in spin–orbit coupled square lattices, New J. Phys. **17**, 073036 (2015).

[41] M. Kawano and C. Hotta, Phase diagram of the square-lattice Hubbard model with Rashba-type antisymmetric spin-orbit coupling, Phys. Rev. B **107**, 045123 (2023).

[42] V. Brosco, D. Guerci, and M. Capone, Pauli metallic ground state in Hubbard clusters with Rashba spin-orbit coupling, Phys. Rev. B **97**, 125103 (2018).

[43] A. Georges, G. Kotliar, W. Krauth, and M. J. Rozenberg, Dynamical mean-field theory of strongly correlated fermion systems and the limit of infinite dimensions, Rev. Mod. Phys. **68**, 13 (1996).

[44] M. Vekić and S. R. White, Pseudogap formation in the half-filled Hubbard model, Phys. Rev. B **47**, 1160(R) (1993).

[45] K. Kubo, Variational Monte Carlo study of ferromagnetism in the two-orbital Hubbard model on a square lattice, Phys. Rev. B **79**, 020407(R) (2009).

[46] A. Greco, M. Bejas, and A. P. Schnyder, Ferromagnetic fluctuations in the Rashba-Hubbard model, Phys. Rev. B **101**, 174420 (2020).

[47] Y. Yanase and M. Sigrist, Superconductivity and magnetism in non-centrosymmetric system: Application to CePt$_3$Si, J. Phys. Soc. Jpn. **77**, 124711 (2008).

[48] J. E. Hoffman, Spectroscopic scanning tunneling microscopy insights into Fe-based superconductors, Rep. Prog. Phys. **74**, 124513 (2011).

[49] H.-M. Guo and M. Franz, Theory of quasiparticle interference on the surface of a strong topological insulator, Phys. Rev. B **81**, 041102(R) (2010).

[50] Y.-Y. Zhang, C. Fang, X. Zhou, K. Seo, W.-F. Tsai, B. A. Bernevig, and J. Hu, Quasiparticle scattering interference in superconducting iron pnictides, Phys. Rev. B **80**, 094528 (2009).

[51] A. Kanigel, M. R. Norman, M. Randeria, U. Chatterjee, S. Souma, A. Kaminski, H. M. Fretwell, S. Rosenkranz, M. Shi, T. Sato, T. Takahashi, Z. Z. Li, H. Raffy, K. Kadowaki, D. Hinks, L. Ozyuzer, and J. C. Campuzano, Evolution of the pseudogap from Fermi arcs to the nodal liquid, Nat. Phys. **2**, 447 (2006).

[52] D. K. Singh, S. Kadge, Y. Bang, and P. Majumdar, Fermi arcs and pseudogap phase in a minimal microscopic model of d-wave superconductivity, Phys. Rev. B **105**, 054501 (2022).

[53] J. Wang, Antiferromagnetic Dirac semimetals in two dimensions, Phys. Rev. B **95**, 115138 (2017).

[54] M. V. Berry, Quantal phase factors accompanying adiabatic changes, Proc. R. Soc. London, Ser. A **392**, 45 (1984).

[55] K. Wakabayashi, M. Fujita, H. Ajiki, and M. Sigrist, Electronic and magnetic properties of nanographite ribbons, Phys. Rev. B **59**, 8271 (1999).

[56] B. A. Bernevig and T. L. Hughes, *Topological Insulators and Topological Superconductors* (Princeton University Press, Princeton, NJ, 2013).

[57] A. Lau and C. Timm, Topological surface states in paramagnetic and antiferromagnetic iron pnictides, Phys. Rev. B **88**, 165402 (2013).

[58] B. Q. Lv, H. M. Weng, B. B. Fu, X. P. Wang, H. Miao, J. Ma, P. Richard, X. C. Huang, L. X. Zhao, G. F. Chen, Z. Fang, X. Dai, T. Qian, and H. Ding, Experimental discovery of Weyl semimetal TaAs, Phys. Rev. X **5**, 031013 (2015).

[59] J. E. Hoffman, K. McElroy, D.-H. Lee, K. M. Lang, H. Eisaki, S. Uchida, and J. C. Davis, Imaging quasiparticle interference in Bi$_2$Sr$_2$CaCu$_2$O$_{8+\delta}$, Science **297**, 1148 (2002).

[60] P. Roushan, J. Seo, C. V. Parker, Y. S. Hor, D. Hsieh, D. Qian, A. Richardella, M. Z. Hasan, R. J. Cava, and A. Yazdani, Topological surface states protected from backscattering by chiral spin texture, Nature (London) **460**, 1106 (2009).

[61] A. Farrell, M. Beaudry, M. Franz, and T. Pereg-Barnea, Quasiparticle interference patterns in a topological superconductor, Phys. Rev. B **91**, 134510 (2015).

[62] S. M. Young and C. L. Kane, Dirac semimetals in two dimensions, Phys. Rev. Lett. **115**, 126803 (2015).

[63] P. G. Matveeva, D. N. Aristov, D. Meidan, and D. B. Gutman, Edge states in a two-dimensional nonsymmorphic semimetal, Phys. Rev. B **99**, 075409 (2019).

[64] P. Richard, K. Nakayama, T. Sato, M. Neupane, Y.-M. Xu, J. H. Bowen, G. F. Chen, J. L. Luo, N. L. Wang, X. Dai, Z. Fang, H. Ding, and T. Takahashi, Observation of Dirac cone electronic dispersion in BaFe$_2$As$_2$, Phys. Rev. Lett. **104**, 137001 (2010).

[65] X. Wan, A. M. Turner, A. Vishwanath, and S. Y. Savrasov, Topological semimetal and Fermi-arc surface states in the electronic structure of pyrochlore iridates, Phys. Rev. B **83**, 205101 (2011).

[66] G. Goyal and D. K. Singh, Semimetallic spin-density wave state in iron pnictides, J. Phys.: Condens. Matter **35**, 365501 (2023).

[67] H. A. Rashid and D. K. Singh, Thermal evolution of the single-particle spectral function in the half-filled Hubbard model and pseudogap, Phys. Rev. B **107**, 125139 (2023).

[68] H. A. Rashid and D. K. Singh, Effect of next-nearest neighbor hopping on the single-particle excitations at finite temperature, SciPost Phys. **16**, 107 (2024).

[69] A. Singh, A systematic diagrammatical treatment of the Hubbard model, Phys. Rev. B **43**, 3617 (1991).